Large Eddy Simulations of high amplitude self-sustained acoustic oscillations in a rocket engine coaxial injector in the transcritical regime

Schmitt Thomas, A Coussement, S. Ducruix, S. Candel

Large Eddy Simulations of high amplitude self-sustained acoustic oscillations in a rocket engine coaxial injector in the transcritical regime

T. Schmitt[a,*], A. Coussement[a], S. Ducruix[a], S. Candel[a]

[a] *Laboratoire EM2C, CNRS, CentraleSupélec, Université Paris-Saclay, Grande Voie des Vignes, 92295 Chatenay-Malabry cedex, France*

Abstract

Understanding the flame dynamics in combustion chambers is still an important field of research. Under certain conditions large amplitude instabilities can occur, leading to degraded operating conditions or even fatal damage to the system. When considering liquid rocket engines (LRE), the power density inside the thrust chamber is so high that when these oscillations take place, they usually lead to the rapid destruction of the engine. In order to avoid this, extensive experimental testing is employed, due to the lack of reliable predictive simulation tools. However, numerical tools represent a promising, faster and cheaper alternative, but further modeling efforts and validations are required to exploit their potential. Stable, steady transcritical flames and transcritical flames modulated by external transverse acoustic waves were successfully simulated recently. However, the ability of computer codes to predict naturally unstable cases, where oscillations are self-sustained must be verified, using well controlled experiments. In this context, JAXA has developed a test bench with a single injector exhibiting large amplitude self-sustained pressure oscillations under certain operating conditions. Depending on the injection parameters and injector geometry, the transcritical flame was found to be stable or unstable. This provides a potentially rich configuration for numerical tools validation. In the present study two cases have been simulated using the AVBP-RG solver jointly developed by CERFACS and EM2C. The first case corresponds to experimentally stable injection conditions, while the second features large pressure oscillations in the chamber. Simulation results feature a higher unsteadiness, with larger fluctuations in the unstable case compared to the stable one, in good qualitative agreement with experimental data. Simulations also indicate that strong interactions take place between the exit nozzle and large-scale entropy fluctuations produced at the end of the flame. This may explain the generation of acoustic waves at this downstream boundary and this process may be at the origin of the coupling loop. In the current state of our simulations, a possible scenario for the triggering of the instability and the associated analysis are described.

Keywords: LES, transcritical combustion, high-frequency combustion instability

1. Introduction

Combustion instabilities have often hindered developments of Liquid Rocket Engines (LRE). Such extreme dynamical phenomena were experienced in many high performance engines. It took a considerable amount of testing to eliminate high frequency instabilities arising in the F-1 engine of the Saturn V rocket [1]. Such instabilities were also encountered during the Ariane development program leading to the in-flight destruction of the second launcher on November 23, 1980. Much of the theoretical understanding and experimental data acquired during the early period are synthesized in [2] while more recent advances are reviewed in [3–5].

The present research project aims at advancing the state of the art in this field by exploring the possibilities of Large-Eddy Simulations (LES) to predict the flame / acoustic dynamics and the resulting combustion instabilities. Simulations reported in what follows correspond to operating conditions prevailing in LREs. The mean chamber pressure exceeds the critical pressure of the liquid oxygen ($p_c(O_2)$ = 5.04 MPa) which is injected at a temperature well below its critical value $T_c(O_2)$ = 154 K. Under these transcritical conditions, the working fluid state departs from that of a perfect gas [6], surface tension vanishes and mass transfer from the dense oxygen stream to the lighter surrounding stream is essentially governed by turbulent production of surface area and mixing. Combustion thus takes place in a complex flow featuring large density gradients and its simulation raises considerable physical and mathematical difficulties.

The flame structure under transcritical conditions is now well documented, for example in [7–13]. In the past decade, efforts have been made to establish computational methodologies for transcritical injection and combustion including real gas thermodynamics, transport models and modified algorithms for numerical integration. LES of turbulent transcritical jets and jet flames have been carried out in the transcritical range by different research groups ([14–25]).

The experimental configuration simulated in the present study, developed by JAXA [26, 27], consists in a single coaxial oxygen / hydrogen injector where large amplitude self-sustained pressure oscillations were observed. Depending on the injection conditions and the geometry of the injector, the flame can be made unstable or not. It is therefore a potentially rich configuration for validation of simulation tools. The experimental setup is briefly described in Sec. 2. The LES solver and the numerical configuration used in the present investigation are reported in Sec. 3. Results obtained on a coarse mesh for the two studied cases are first briefly presented in Sec. 4. Attention is focused on the unsta-

*Corresponding author

Email address: thomas.schmitt@centralesupelec.fr (T. Schmitt)

ble case in Sec. 5, where simulations on a finer grid are presented together with an analysis of the flow dynamics.

2. Brief description of the experimental setup

2.1. JAXA's test bench

The experimental setup, operated by JAXA, is presented in detail in [26, 27]. It consists in a coaxial LOx / H_2 injector. Transcritical oxygen is injected through the inner injector, surrounded by gaseous hydrogen. A sketch of the chamber is shown in Fig. 1. The cylindrical chamber is equipped with dynamic and static pressure transducers to measure mean pressure and time resolved pressure fluctuations. The chamber walls are water-cooled and heat flux measurements are available. The injector is characterized by its thin lip and annular channel characteristic size (0(1 mm)) compared with the chamber length (0(100 mm)). The chamber ends with a choked nozzle.

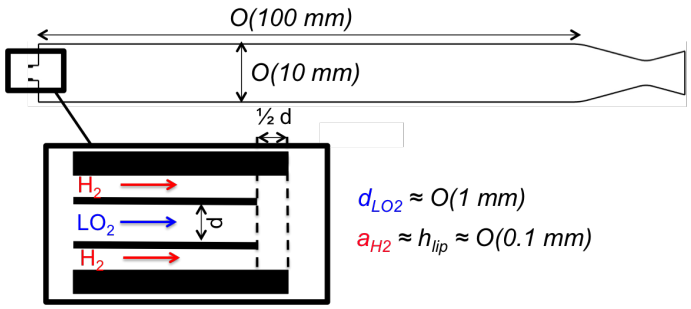

Figure 1: Schematic representation of the experimental setup. d_{LO2} stands for the oxygen injector diameter, a_{H_2} is the annular injector width and h_{lip} is the injector lip thickness.

2.2. Chosen operating points

Injection conditions for the two selected cases are given in Tab. 1. All the values are normalized by those from case 1. The two cases correspond to the same mass flow rates of oxygen and hydrogen and the oxygen injection temperature is kept constant. The final pressure in the chamber is also close for the two cases. The hydrogen temperature significantly changes between the two cases. The reduced injection temperature for case 2 leads to a lower injection velocity compared with case 1, decreasing the momentum flux ratio between the two fluids. In both cases operation takes place in the transcritical regime : pressure is higher than the critical pressure of both fluids while injection temperature for oxygen is lower than its critical value. Under such conditions, oxygen density and thermodynamic state at injection are close to those of a liquid while hydrogen is gaseous.

Power spectral densities (PSDs) of the experimental dynamic pressure measurements are shown on Fig. 2 for cases 1 and 2 on the datasets provided by JAXA. The spectral analysis is performed using Welch's periodogram method by averaging PSDs over an ensemble of 50 blocks with a final frequency resolution of 250 Hz. While both cases feature two frequency peaks between 2.0 and 2.5 kHz and 4.0 and 4.5 kHz, corresponding to the first and second longitudinal modes of the chamber, pressure fluctuation amplitude is much larger for case 2. In particular, a peak at 2.4 kHz clearly dominates the spectrum for case 2 and this case is considered as being unstable while case 1 is stable. Both cases feature a low frequency content around 350 Hz.

Case	$T^*_{H_2}$ [-]	$T^*_{LO_2}$ [-]	$\dot{m}^*_{H_2}$ [-]	$\dot{m}^*_{LO_2}$ [-]	$P*_{ch}$ [-]
1	**1**	1	1	1	1
2	**0.71**	0.97	1.05	0.95	0.99

Table 1: Operating points chosen for the simulation. All the data are normalized by the values for case 1. P_{ch} is the chamber mean pressure, $\dot{m}_{LO_2}$ and $\dot{m}_{H_2}$ are the mass flow rates of oxygen and hydrogen respectively. The injection temperatures for oxygen and hydrogen are T_{LO_2} and T_{H_2} respectively. All the operating parameters are kept nearly constant between both cases, only the hydrogen injection temperature is changed while maintaining the mass flow rate $\dot{m}^*_{H_2}$. The pressure in the chamber is higher than the critical pressure of oxygen and hydrogen. Oxygen is injected in transcritical conditions (temperature lower than the critical temperature).

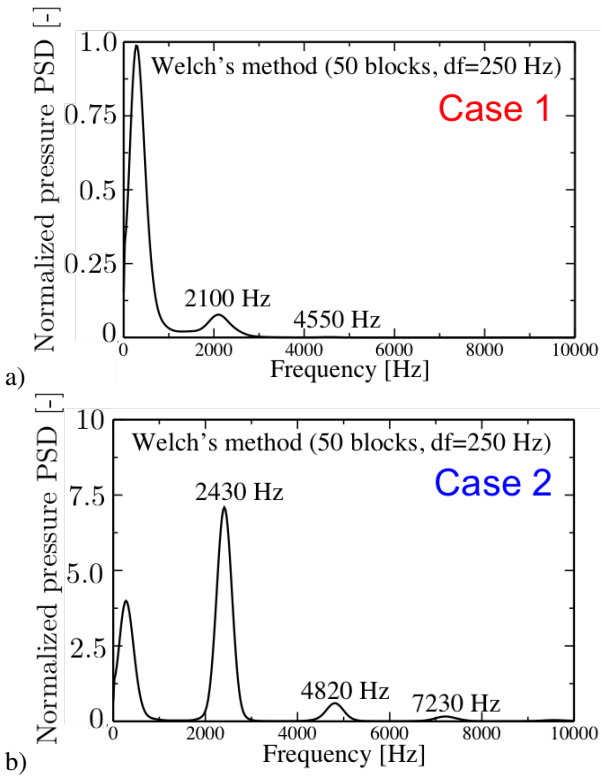

Figure 2: *Experimental measurements* Power spectral density of experimental pressure (the sensor is located at the injection plan). (a) Case 1 (b) Case 2. Adapted from [27].

3. Numerical setup

3.1. Large-Eddy Simulation solver

The unstructured AVBP compressible flow solver (see among others [28, 29]) is used in what follows to integrate the three-dimensional compressible Navier-Stokes equations for a multi-component mixture of reactive fluids. The numerical method uses a low-dissipation centered scheme, third-order in space and time [30]. Boundary conditions are treated with the characteristic wave decomposition method NSCBC [31]. A real-gas version of the AVBP flow solver, called AVBP-RG, was recently developed [32, 33] with appropriate models to account for real-gas

non-idealities. The Soave-Redlich-Kwong equation of state [34] was included in the solver:

$$p = \frac{\rho r T}{1 - \rho b_m} - \frac{\rho^2 a_m(T)}{1 + \rho b_m} \quad (1)$$

with T the temperature and $r = \mathcal{R}/W$, where $\mathcal{R}$ designates the universal gas constant and W is the molar mass. The coefficients $a_m(T)$ and b_m are calculated according to [35]. Equation (1) is used for a consistent derivation of the pressure dependence of thermodynamic properties (internal energy, enthalpy, specific heats, compressibility), as described in [35, 36]. Chemical conversion is handled using an infinitely fast chemistry model presented in [22]. NSCBC boundary conditions are adapted to real-gas thermodynamics [37]. Because of the steep density and internal energy gradients, real-gas simulations require a specific numerical stabilization procedure described in [33]. The WALE model [38] is used to represent the sub-grid scale (SGS) shear stress tensor. The SGS energy and species fluxes are modeled using gradient transport assumptions with sub-grid Prandtl and Schmidt numbers set to 0.7. Results of calculations in high pressure transcritical cases indicate that the AVBP-RG flow solver in combination with these models provides solutions which are in good agreement with experimental data [22–25], giving us confidence in the capability of the solver to examine transcritical combustion dynamics problems.

3.2. Numerical configuration

Calculations are carried out in the exact configuration used in the experimental investigation on JAXA's test-bench. The numerical domain is shown in Fig. 3. The outlet nozzle is included in the domaine to ensure a representative exit condition, on the aerodynamic as well as on the acoustic points of view. Two meshes are employed in this study (Tab. 2). The coarse grid was used for first simulations in order to characterize the main features of each case. Case 2 is then simulated on the finer grid. The cell distribution for each grid is shown in Fig. 4. For both cases, 7 cells are used to discretize the injector lip. The grid resolution is improved in the chamber for the finer grid where a constant cell size is kept from the backplane to the exit section. This meshing strategy differs from the one used for the coarse grid, where it is slowly increasing in the axial direction.

Mesh	Nb of nodes	Nb of tetrahedra
Coarse	2 500 000	12 500 000
Fine	6 000 000	30 000 000

Table 2: Main characteristics of the two meshes used in this study.

Walls are treated with an adiabatic no-slip condition in the injection manifold and an anisotropic turbulence is injected at the inlet following the methodology described in [39]. Bulk and rms profiles, resulting from an independent LES of a long tube with the same Reynolds number and mesh resolution, are used to impose velocity conditions at the injector channels. Heat losses at the chamber walls are accounted for using isothermal law of the wall. A wall temperature of 500 K is chosen here, in order to keep a reasonable agreement with the heat losses measured experimentally during hot-fire tests.

4. Results on coarse grid

This section is intended to provide a brief description of results obtained using the coarse grid for the two cases under investigation. These calculations serve as a first characterization of the two flows. It is shown in particular that both flames have a similar behavior, except that the one corresponding to case 2 is slightly longer. Both cases feature large scale variations at the end of the chamber, and strong interaction with the outlet nozzle. The unstable regime (case 2) will be examined on the fine grid.

4.1. Brief description of the flow field

Longitudinal slices of instantaneous oxygen mass fraction and temperature are shown in Fig. 5. In both cases, the flow produces a long flame that fills the whole chamber. Despite the limited grid resolution in the second part of the chamber, strong unsteadiness is captured. Large scale oxygen pockets are created at the end of the flame. Oxygen rich zones eventually persist until the end of the chamber, interacting with the outlet nozzle and leading to large temperature fluctuations in the nozzle. Average fields (not shown here) indicate that case 2 produces a slightly longer flame compared to case 1 (the flame length is about 10 % longer). Differences between the two cases in terms of flow structure are nevertheless limited.

4.2. Pressure measurement and discussion

A sample of the temporal evolution of pressure is plotted in Fig. 7 for cases 1 and 2. Both cases feature bursts of pressure fluctuations. These pressure events are also observed in the experiment for case 1 (not shown here). While pressure fluctuation amplitude is larger in case 2 than in case 1, the very large amplitude fluctuations expected from the experimental results are not retrieved. Instead the pressure fluctuations are rapidly damped. For both cases, the dominant frequency corresponds to the first longitudinal mode, in agreement with experimental results. The pressure noise that is observed in both cases is attributed to the interaction between the flow and the outlet nozzle accordingly to [40] and is more likely to occur in case 2 as the flame is longer.

As interaction between the flow and the nozzle play a significant role in the occurrence of the instability, case 2 is now studied on a finer grid with an improved grid resolution in the chamber.

5. Unstable case on fine grid

The detailed analysis of the unstable case is now carried out on the fine grid.

5.1. Flame geometry

Longitudinal slices of instantaneous oxygen mass fraction and density are shown in Fig. 8. The inner high density oxygen jet shows a limited initial spreading angle and extends to the middle of the domain. The jet eventually destabilizes forming large scale pockets of oxygen. These high density pockets are wrinkled by the surrounding turbulence and finally "dissolved" in the last part of the chamber. As observed in the coarse grid simulations, some unreacted oxygen pockets reach the exhaust nozzle. Strong shear is generated close to the injector by the annular high velocity hydrogen flow (Fig. 9)a. This region is characterized by intense

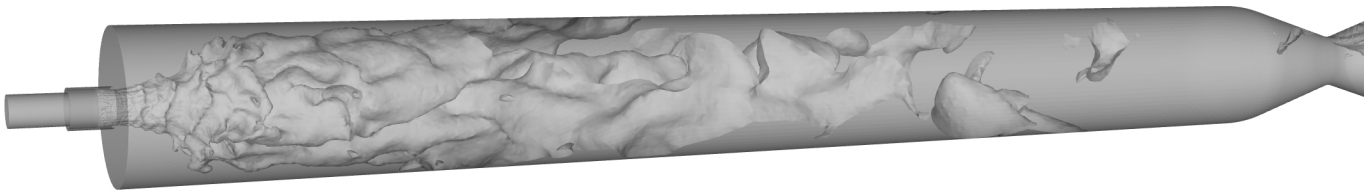

Figure 3: Full 3D geometry used in the simulations. As an illustration, a temperature iso-surface is added.

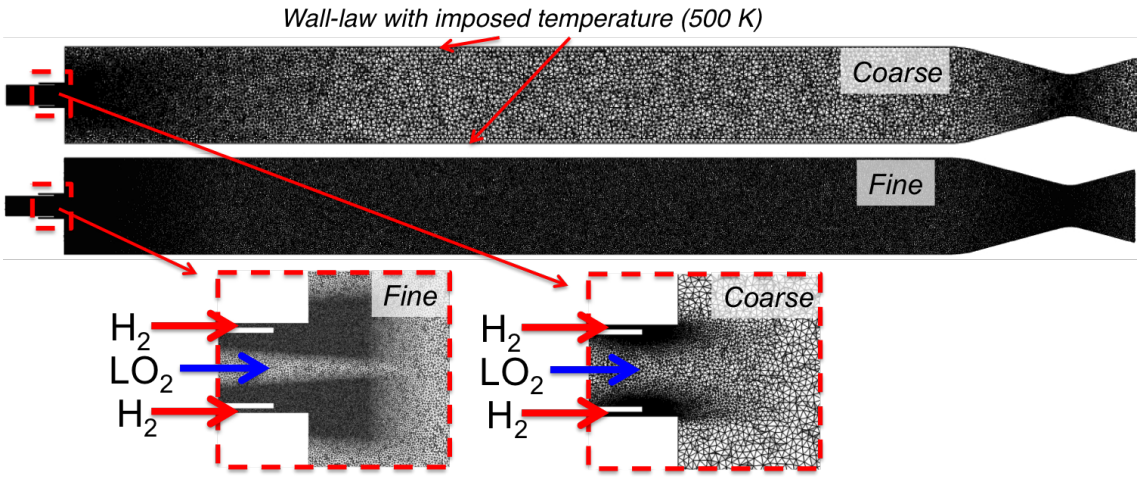

Figure 4: Coarse and fine meshes used in this study.

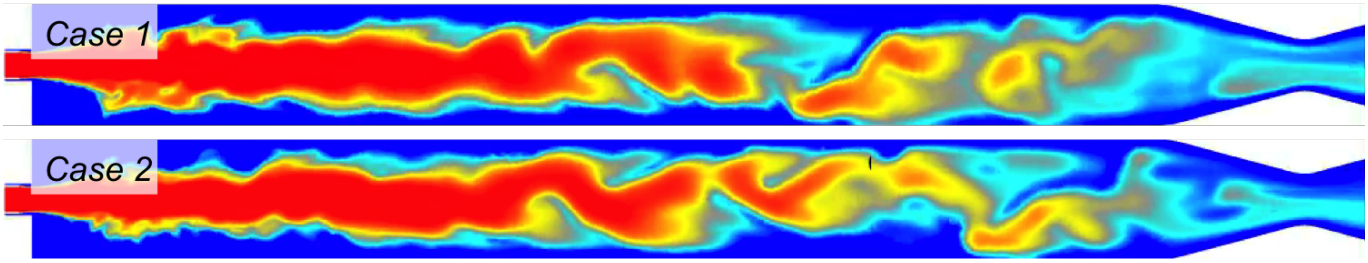

Figure 5: *LES results on coarse grid.* Longitudinal slice of instantaneous oxygen mass fraction (red: 1 ; blue: 0).

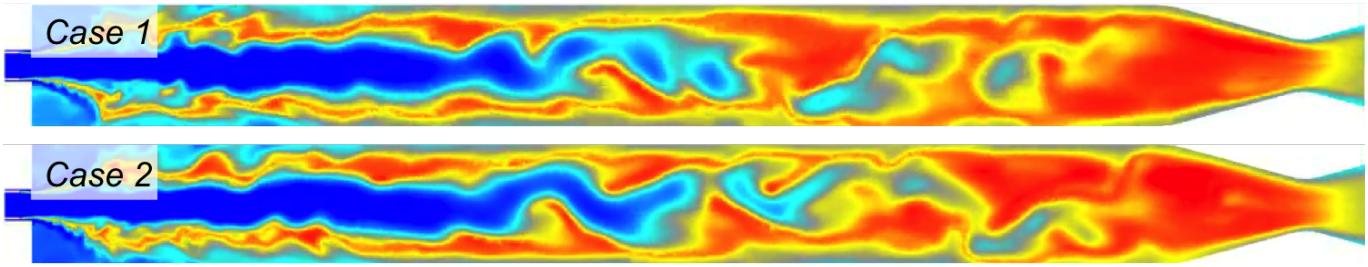

Figure 6: *LES results on coarse grid.* Longitudinal slice of instantaneous temperature (red: 3 600 K ; blue: 100 K).

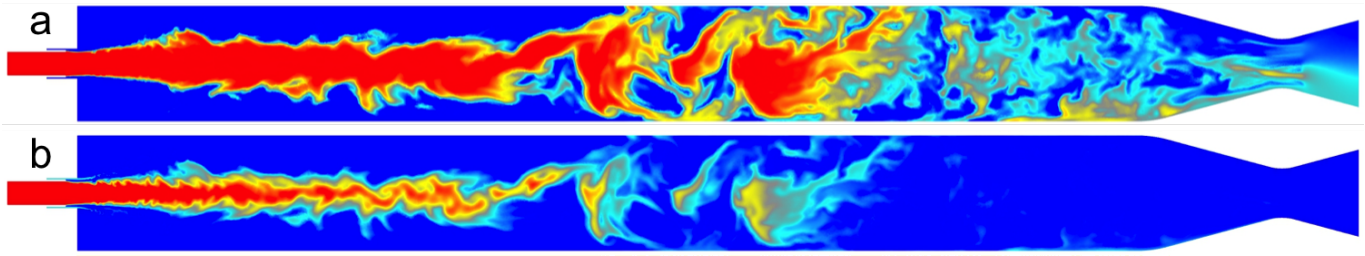

Figure 8: *LES results on fine grid*. Longitudinal slice of instantaneous (a) oxygen mass fraction and (b) density (in logarithmic scale). Blue: minimum, red: maximum.

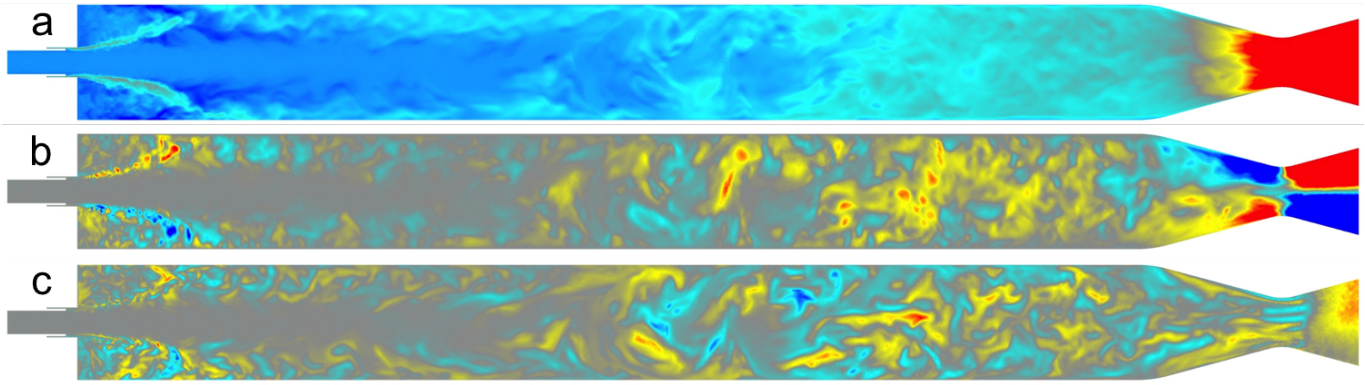

Figure 9: *LES results on fine grid*. Longitudinal slice of instantaneous (a) axial, (b) radial and (c) azimuthal velocity. Blue: minimum (O(-100 m/s)), red: maximum (O(100 m/s)).

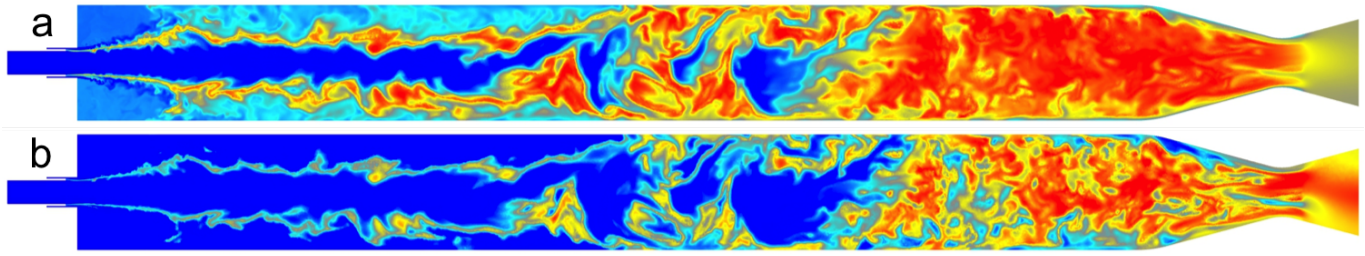

Figure 10: *LES results on fine grid*. Longitudinal slice of instantaneous (a) temperature and (b) OH mass fraction. Blue: minimum, red: maximum.

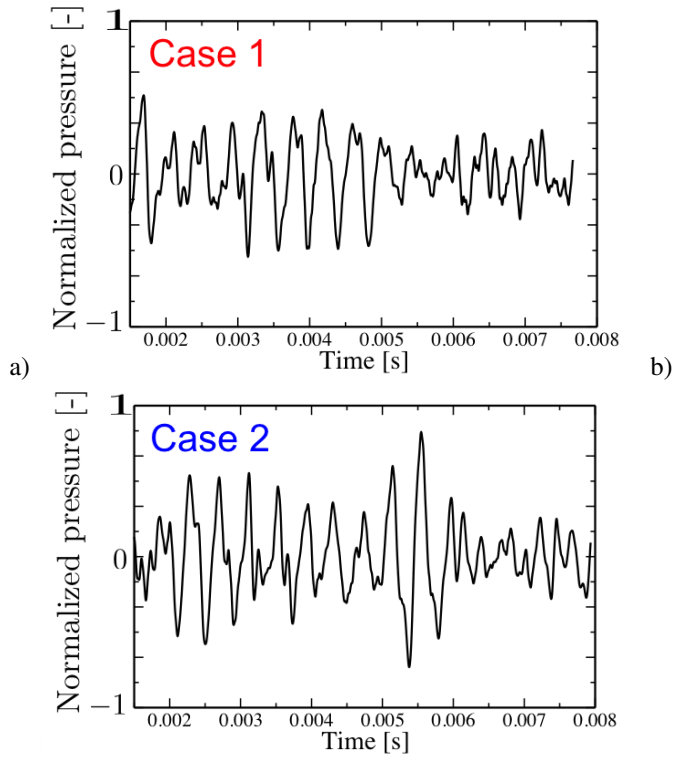

Figure 7: *LES results on coarse grid*. Temporal evolution of pressure fluctuations (located at the injection plan). (a) Case 1, (b) Case 2.

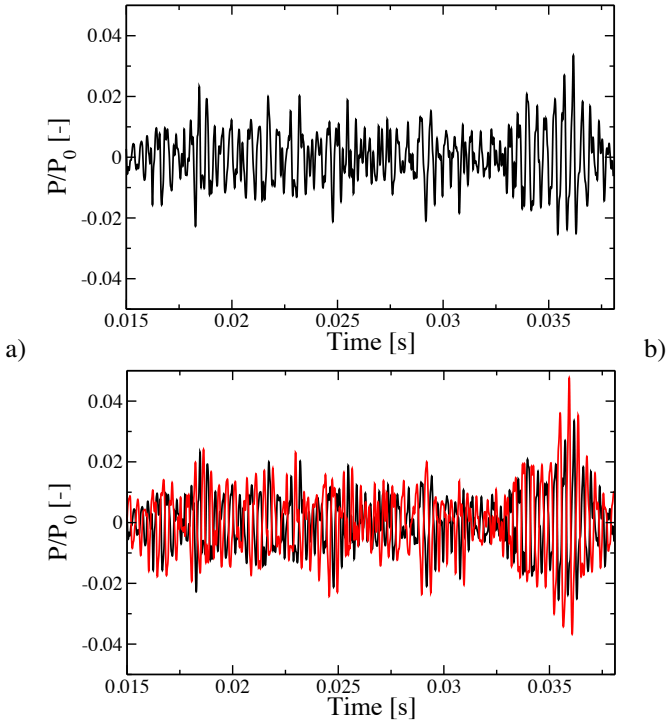

Figure 11: *LES results on fine grid* (a) Temporal evolution of pressure in the near injector region. (b) Temporal evolution of pressure in the near injector region (black) and close to the nozzle (red).

small size vortices. As the flow approaches the chamber walls, larger scale vortices are generated around the inner oxygen jet (Fig. 8)b. This phenomenon is promoted by the confinement of the flame by the lateral walls, also creating a large scale recirculation zone between the inner high density jet and the annular flow (Fig. 9)a. Further downstream, a highly turbulent flow is visible in the wake of the inner jet (Fig. 9). This flow mixes oxygen with surrounding gases and combustion is enhanced (Fig. 10). A flame geometry similar to the one observed on the coarse grid is retrieved. As expected, the second part of the jet features much more resolved turbulence scales with the fine grid.

5.2. Pressure evolution

Figure 11 displays the pressure signal in the near injector region. Fluctuation amplitudes are limited and still lower than those measured experimentally. Events of pressure peaks that can reach 3 % of the mean pressure are nevertheless noticeable. These fluctuations are generally rapidly damped, but may last for several periods (see for example pressure fluctuations around 0.035 s on Fig. 11). Figure 11b shows the temporal evolution of pressure both in the near injector region and close to the nozzle exit. The signals are clearly in phase opposition for the full simulation sequence, indicating that these oscillations correspond to the first longitudinal mode of the chamber. This is in agreement with the experimental observations.

In the power spectral density of the pressure detected by the two probes (Fig. 12) a dominant frequency appears around 2.4 kHz, and two other peaks are found at 4.9 kHz and 7.25 kHz. These frequencies are also in good agreement with experimental measurements. From these LES results, it seems that the acoustic fluctuations observed experimentally for case 2 are reproduced by the calculation even though the final amplitude is lower than that observed in the experiment.

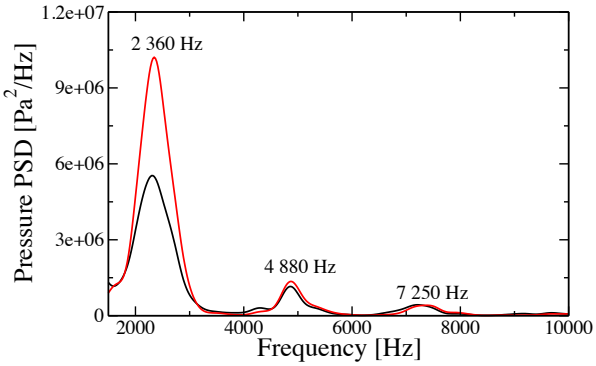

Figure 12: *LES results on fine grid* Power spectral density of pressure in the near injector region (black) and at the nozzle (red). Welch's method with an averaging over 5 blocks and a spectral resolution of 220 Hz.

5.3. Flame dynamics

It is next instructive to examine the flame dynamics during one period of oscillation. The period chosen corresponds to a maximum of pressure fluctuation amplitude measured in the simulation (indicated by 1, 2 and 3 on Fig. 13a). Three successive instants over one period are shown in Fig. 13b. The large amplitude variations of pressure that corresponds to the first longitudinal mode are clearly observable.

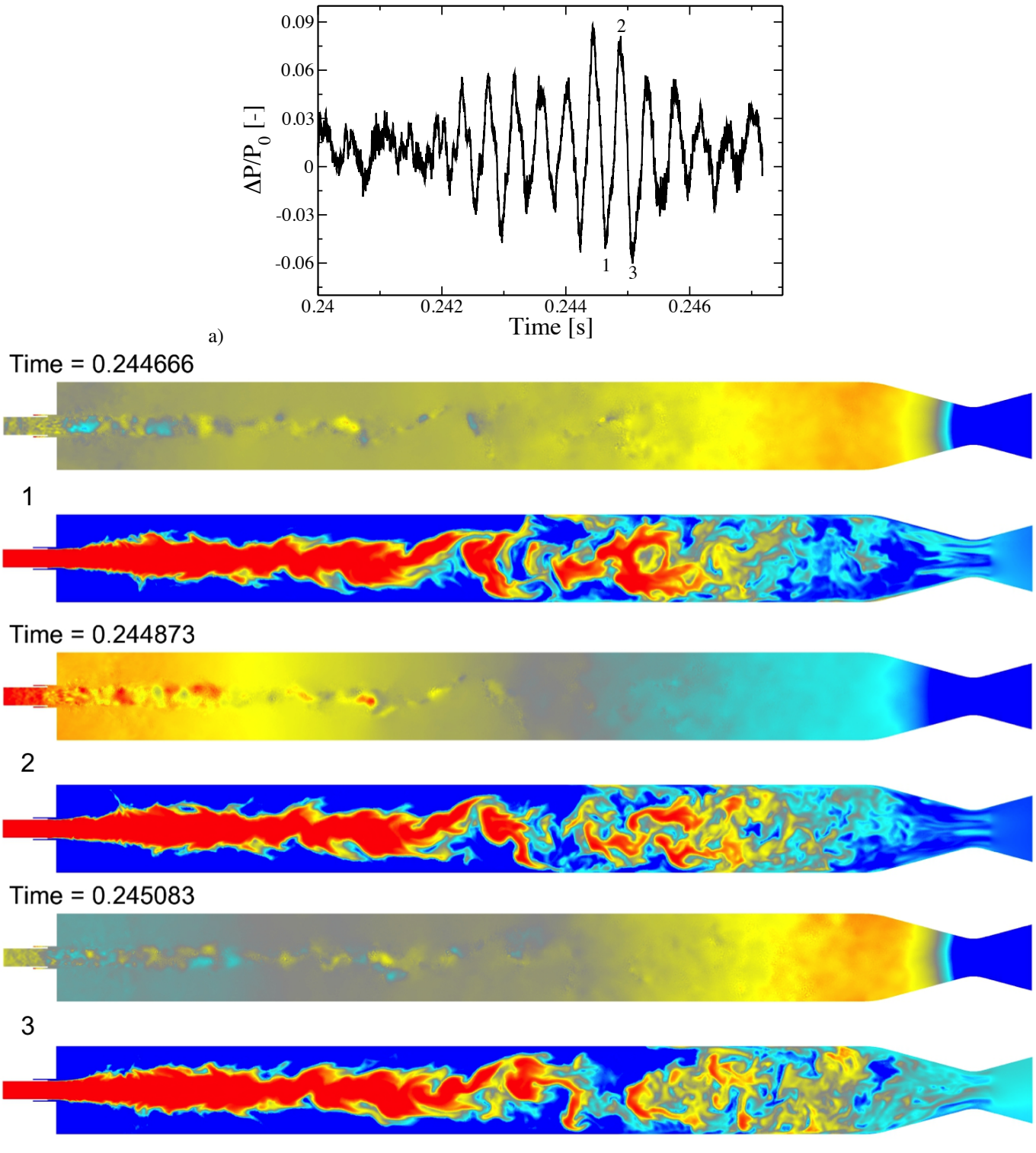

Figure 13: *LES results on fine grid*. (a) Temporal evolution of the difference between the pressure in the near injector region and at the nozzle (ΔP). (b) Three successive instants over one period of oscillation. Longitudinal slice of instantaneous pressure (top) and O2 mass fraction (bottom). Blue: minimum, red: maximum.

5.4. Acoustic energy balance and heat release rate fluctuations

It is now interesting to consider the acoustic energy balance in the thrust chamber and to this purpose examine heat release rate fluctuations. It is known that the unsteady heat release rate $\dot{q}'$ participates in the acoustic source term in the acoustic energy balance and constitutes the driving source of combustion instabilities. It is instructive to recall this balance equation. As a first step, the speed of sound will be considered as constant, and the flow effect negligible:

$$\frac{\partial \mathcal{E}}{\partial t} + \boldsymbol{\nabla} \cdot \boldsymbol{\mathcal{F}} = \mathcal{S} - \mathcal{D} \tag{2}$$

In this expression $\mathcal{E}$, $\boldsymbol{\mathcal{F}}$, $\mathcal{S}$ and $\mathcal{D}$ represent the acoustic energy density, acoustic energy flux, volumetric source term and volumetric damping in the domain with:

$$\mathcal{E} = \frac{1}{2}\frac{p'^2}{\rho_0 c^2} + \frac{1}{2}\rho_0 v'^2 \tag{3}$$

$$\boldsymbol{\mathcal{F}} = p'\boldsymbol{v}' \tag{4}$$

$$\mathcal{S} = \frac{\gamma - 1}{\rho_0 c^2} p'\dot{q}' \tag{5}$$

The damping term that appears in the balance equation (2) is less easy to write explicitly because it covers a variety of processes reducing the acoustic energy. Examining the previous expressions one observes that the heat release rate appears in the right hand side in the form of a product with the pressure. The source term will be positive if the instantaneous product $p'q'$ is positive. This corresponds to the Rayleigh criterion [41]. According to this criterion an instability may occur if the pressure and heat release rate fluctuations are in phase. This is only a necessary condition. Integrating the local balance of acoustic energy over a period of oscillation $T = 2\pi/\omega$ and over the volume of the chamber one finds

$$\frac{d}{dt}\int_V E dV + \int_A \boldsymbol{F}\cdot\boldsymbol{n} = \frac{\gamma-1}{\rho_0 c^2}\int_V \frac{1}{2}\mathrm{Re}\{p'\dot{q}'\}dV - \int_V D dV \tag{6}$$

The acoustic energy will actually grow if the source term is greater than the damping term plus the integrated outgoing acoustic fluxes crossing the boundaries of the domain :

$$\frac{\gamma-1}{\rho_0 c^2}\int_V \frac{1}{2}\mathrm{Re}\{p'\dot{q}'\}dV > \int_V D dV + \int_A \boldsymbol{F}\cdot\boldsymbol{n} \tag{7}$$

To examine the source term one may first look at the time evolution of the fluctuation of heat release rate integrated over the whole domain

$$\dot{Q}' = \int \dot{q}' dV \tag{8}$$

This quantity is plotted in Fig. 14a. Similarly to pressure, events of heat release rate fluctuations are observed during the simulation. The amplitude of these oscillations are around 5 % and reach up to 10 % of the mean value. These fluctuations occur at the same frequency as the pressure (Fig. 14b) and one may conclude that pressure oscillations generate heat release rate fluctuations in the system.

It is next interesting to examine the temporal signals of pressure and heat release rate fluctuations plotted in Fig. 15. Attention is given to the phase between $\dot{Q}'$ and the acoustic pressure

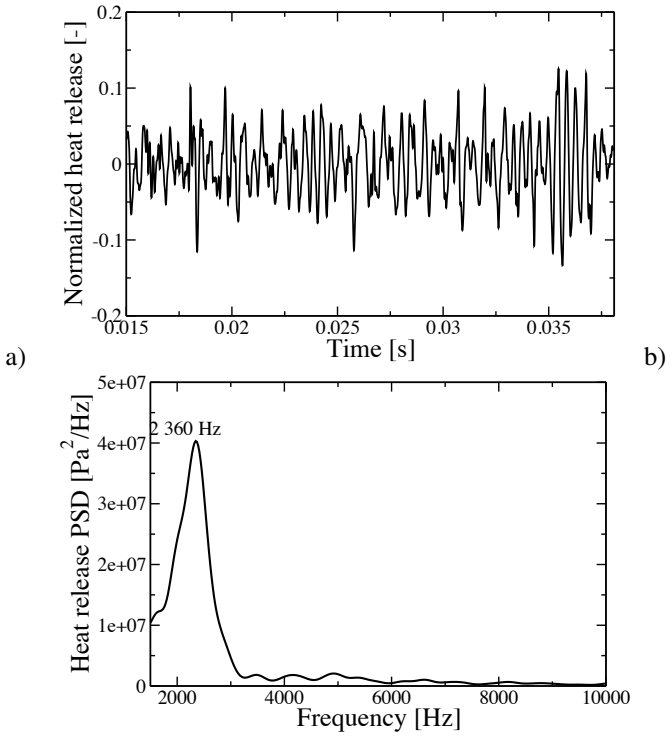

Figure 14: *LES results on fine grid* (a) Temporal evolution of heat release rate fluctuations. (b) Power spectral density of heat release rate. Welch's method with 5 blocks and a spectral resolution of 220 Hz.

p' at the injector vicinity and at the exhaust section. One finds that $\dot{Q}'$ is out of phase with respect to p'_{in} but is nearly in phase with the pressure at the nozzle exhaust p'_{noz}. It is now clear that in the estimation of the Rayleigh source term one has to account for the axial variation of the pressure field and heat release rate integrated over the chamber cross section. This requires these two spatial distributions to be extracted from the corresponding signals by filtering around the frequency of oscillation of the resonant mode involved in the unstable oscillation. This procedure will be explored in a near future.

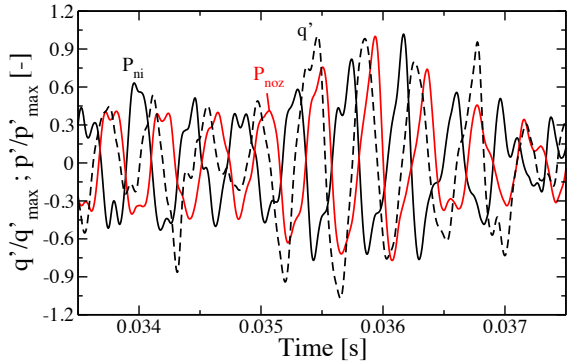

Figure 15: *LES results on fine grid* Temporal evolution of pressure at the near-injector probe (P_{ni}), near-nozzle probe (P_{noz}) and heat release fluctuations q' for case 2.

6. Conclusion

This article describes recent advances in the simulation of a naturally unstable transcritical coaxial injector. The experimental configuration, operated by JAXA, can be made unstable or not depending on the injection conditions and the geometry of the injector. Two cases are considered for which only temperature varies, one being stable (case 1) and the other one featuring large amplitude pressure oscillations (case 2).
The two cases are first calculated on a coarse grid, where the main flow structures and dynamics are identified. They both feature a long flame, that fills a large part of the chamber, and show regular release of large scale cold oxygen pockets that may eventually interact with the exit nozzle. Harmonic pressure fluctuations are present in both cases. In particular, bursts of higher amplitude pressure fluctuations are regularly observed, especially for case 2. Nevertheless, the amplitude of pressure fluctuation is much lower than in the experiment for case 2. The two cases finally present a similar behavior, with a flame slightly longer for case 2 compared with case 1. It is assumed that this difference promotes flame / nozzle interaction for case 2, a scenario that could explain the larger pressure fluctuation measured experimentally in that situation.
From these results, case 2 is calculated on a finer mesh, where the characteristic mesh size is strongly refined in the chamber. While pressure oscillation amplitudes are still lower than those measured experimentally, the pressure field corresponds to the first longitudinal mode and the calculated frequencies are in good agreement with experiments. A first analysis of the heat release rate fluctuations indicates a limited coupling between combustion and acoustics in the acoustic energy balance in this simulation. It is currently believed that flame / nozzle interaction may play a role in the instability process. Current studies are focused on the detailed acoustic analysis of the strong unstable event found at the end of the simulation and illustrated in this document.

Acknowledgements

This work is supported by SAFRAN Snecma Space Engines Division, the prime contractor of the Ariane launcher cryogenic propulsion system and CNES, the French National Space Agency. Dr Yoshio Nunome (JAXA) is gratefully acknowledged for providing us the experimental data. This work was granted access to the HPC resources of IDRIS and CINES made available by GENCI (Grand Equipement National de Calcul Intensif) under the allocation x20152b6176.

References

[1] J. C. Oefelein, V. Yang, J. Propul. Power 9 (1993) 657–677.

[2] D. T. Harrje, F. H. Reardon, NASA Special Publication 194 (1972).

[3] V. Yang, W. Anderson (Eds.), Liquid Rocket Engine Combustion Instability, volume 169, Progress in Astronautics and Aeronautics, 1995.

[4] F. E. C. Culick, Unsteady Motions in Combustion Chambers for Propulsion Systems, volume RTO-AG-AVT-039 of *RTO AGARDograph*, The Research and Technology Organisation (RTO) of NATO, 2006.

[5] S. Candel, M. Juniper, G. Singla, P. Scouflaire, C. Rolon, Combust. Sci. Technol. 178 (2006) 161–192.

[6] J. Oefelein, Proc. Combust. Inst. 30 (2005) 2929–2937.

[7] M. Juniper, A. Tripathi, P. Scouflaire, J. Rolon, S. Candel, Proc. Combust. Inst. 28 (2000) 1103–1110.

[8] G. Singla, P. Scouflaire, C. Rolon, S. Candel, Proc. Combust. Inst. 30 (2005) 2921–2928.

[9] D. W. Davis, B. Chehroudi, J. Propul. Power 23 (2007) 364–374.

[10] K. Miller, J. Sisco, N. Nugent, W. Anderson, J. Propul. Power 23 (2007) 1102–1112.

[11] Y. Méry, L. Hakim, P. Scouflaire, L. Vingert, S. Ducruix, S. Candel, Compt. Rend. Mécan. 341 (2013) 100–109. Special issue "Combustion for Aerospace Propulsion".

[12] J. S. Hardi, H. C. G. Martinez, M. Oschwald, B. B. Dally, Journal of Propulsion and Power 30 (2014) 337–349.

[13] S. Gröning, J. S. Hardi, D. Suslov, M. Oschwald, Journal of Propulsion and Power (2016) 1–14.

[14] J. C. Oefelein, V. Yang, J. Propul. Power 14 (1998) 843–857.

[15] J. Oefelein, Combust. Sci. Technol. 178 (2006) 229–252.

[16] N. Zong, V. Yang, Combust. Sci. and Technol. 178 (2006) 193–227.

[17] N. Zong, V. Yang, Int. J. Computational Fluid Dynamics 21 (2007) 217–230.

[18] P. Tucker, S. Menon, C. Merkle, J. Oefelein, V. Yang, AIAA Paper 5226 (2008).

[19] G. Ribert, N. Zong, V. Yang, L. Pons, N. Darabiha, S. Candel, Combust. Flame 154 (2008) 319–330.

[20] M. Masquelet, S. Menon, Y. Jin, R. Friedrich, Aerospace Science and Technology 13 (2009) 466–474.

[21] S. Matsuyama, J. Shinjo, S. Ogawa, Y. Mizobuchi, in: 48th AIAA Aerospace Sciences Meeting, Orlando, Florida, pp. 2010–208.

[22] T. Schmitt, Y. Méry, M. Boileau, S. Candel, Proc. Combust. Inst. 33 (2011) 1383–1390.

[23] T. Schmitt, J. Rodriguez, I. A. Leyva, S. Candel, Physics of Fluids 24 (2012).

[24] L. Hakim, A. Ruiz, T. Schmitt, M. Boileau, G. Staffelbach, S. Ducruix, B. Cuenot, S. Candel, Proceedings of the Combustion Institute 35 (2015) 1461–1468.

[25] L. Hakim, T. Schmitt, S. Ducruix, S. Candel, Combustion and Flame 162 (2015) 3482–3502.

[26] Y. Nunome, M. Takahashi, A. Kumakawa, K. Miyazaki, S. Yoshida, T. Onga, AIAA Paper 2008-4848 (2008).

[27] Y. Nunome, T. Onodera, M. Sasaki, T. Tomita, K. Kobayashi, Y. Daimon, AIAA Paper 2011-6027 (2011).

[28] V. Moureau, G. Lartigue, Y. Sommerer, C. Angelberger, O. Colin, T. Poinsot, J. of Comput. Phys. 202 (2005) 710–736.

[29] N. Gourdain, L. Gicquel, M. Montagnac, O. Vermorel, M. Gazaix, G. Staffelbach, M. Garcia, J. Boussuge, T. Poinsot, Computational Science & Discovery 2 (2009) 015003.

[30] O. Colin, M. Rudgyard, J. Comput. Phys. 162 (2000) 338–371.

[31] T. Poinsot, S. Lele, J. Comput. Phys. 101 (1992) 104–129.

[32] L. Pons, N. Darabiha, S. Candel, Combust. Flame 152 (2008) 218–229.

[33] T. Schmitt, L. Selle, A. Ruiz, B. Cuenot, AIAA Journal 48 (2010).

[34] G. Soave, Chemical Engineering Science 27 (1977) 1197–1203.

[35] B. E. Poling, J. M. Prausnitz, J. P. O'Connel, The properties of gases and liquids, McGraw-Hill, fifth edition, 2001.

[36] V. Yang, Proc. Combust. Inst. 28 (2000) 925–942.

[37] N. Okong'o, J. Bellan, J. Comput. Phys. 176 (2002) 330–344.

[38] F. Nicoud, F. Ducros, Flow, Turbulence and Combustion 62 (1999) 183–200. JX.

[39] A. Smirnov, S. Shi, I. Celik, ASME Transactions- Journal of Fluids Engineering 123 (2001) 359–371.

[40] F. E. Marble, S. M. Candel, Journal of Sound and Vibration 55 (1977) 225–243.

[41] B. J. W. S. Rayleigh, The theory of sound, volume 2, Macmillan, 1896.